AIAA-2002-3889

# COMPUTING AXISYMMETRIC JET SCREECH TONES USING UNSTRUCTURED GRIDS

**Philip C. E. Jorgenson and Ching Y. Loh***
National Aeronautics and Space Administration
Glenn Research Center at Lewis Field
Brookpark, Ohio 44135, USA

## Abstract

The space-time conservation element and solution element (CE/SE) method is used to solve the conservation law form of the compressible axisymmetric Navier-Stokes equations. The equations are time marched to predict the unsteady flow and the near-field screech tone noise issuing from an underexpanded circular jet. The CE/SE method uses an unstructured grid based data structure. The unstructured grids for these calculations are generated based on the method of Delaunay triangulation.

The purpose of this paper is to show that an acoustics solution with a feedback loop can be obtained using truly unstructured grid technology. Numerical results are presented for two different nozzle geometries. The first is considered to have a thin nozzle lip and the second has a thick nozzle lip.

Comparisons with available experimental data are shown for flows corresponding to several different jet Mach numbers. Generally good agreement is obtained in terms of flow physics, screech tone frequency, and sound pressure level.

## 1 Introduction

It is desirable to develop a general computer code that can predict the complex flow structure around complicated geometries and the associated aeroacoustics. Many computational fluid dynamics methods have been developed that take advantage of an inherent grid structure which permits flow solutions to be obtained efficiently. For computational aeroacoustics (CAA), another obvious advantage of the structured grid is its well-controlled grid quality (size and shape) that helps to maintain the high quality of the computed acoustic waves. This structure, which makes the solver so efficient, often makes it difficult to generate grids about complex geometries without an additional complication of blocked or overset grid techniques.

An unstructured grid flow solver can alleviate many of the problems associated with structured grids. Unlike a structured grid, the unstructured grid neighborhood must be provided to the solver explicitly. The simplest geometric figure that can cover a two-dimensional domain is the triangle. The advantage of the triangle is that it can easily be used to generate a grid over an arbitrary domain without overlapping. It also has the advantage of clustering in high flow gradient regions without the concern of the surrounding cell structure. The main disadvantage of the unstructured grid is the additional memory requirements in the flow solver to store the grid. More of the burden is placed on the computer code, thus the user input is reduced both during grid generation and flow solution such that more configurations can be tested in a shorter period of time. For CAA, the grid quality of an unstructured grid is less controllable and it may deteriorate the acoustic wave computations. The situation may be even more critical if a complicated acoustic feedback loop is present, which is the problem type considered in this paper.

The problems under consideration in this paper are circular underexpanded supersonic jets [1-8]. These jets radiate a combination of mixing noise, broadband shock-associated noise, and under certain conditions screech tones. Mixing noise from jets can be directly associated with large-scale structures, or instability waves in the shear layer. The broadband shock-associated noise and screech tones are associated with the interaction of these instability waves with shock cell structure in the jet core. The screech tones arise due to a feedback loop, *i.e.*, part of the acoustic waves generated by the instabil-

*Taitech Inc., Member AIAA

ity wave/shock-cell interaction propagate upstream and re-generate the instability waves at, or in the vicinity of, the nozzle lip. The desire to control screech noise is not only due to general noise reduction concerns. It can also cause damage to the structure due to sonic fatigue. The feedback loop is sensitive to small changes such as lip thickness and other phenomena. Most of this understanding comes from experimental observations. Numerical methods that can predict screech tones will help in the understanding and the eventual control of this noise source.

A direct numerical simulation was computed by Shen and Tam [9,10] for screech tones issuing from a circular jet, based on the well-known DRP scheme, with a structured grid. A large computational domain of $35D$ long in the streamwise direction and $17D$ in radial direction was used in their computation, with $D$ being the nozzle diameter.

More recently the space-time conservation element and solution element (CE/SE) method with a triangulated structured grid [11-14] has been used to predict the near-field screech tones from underexpanded supersonic jets [15]. The near-field results compared well with the experimental data, [4-8]. This work also demonstrated the capability of the CE/SE nonreflecting boundary condition. This allows the computational domain to be more compact reducing the overall mesh memory size requirements. The present work is a companion work of [15]. Here a truly unstructured grid, generated by a point insertion Delaunay method rather than a triangulated structured grid, is employed. This is done with the idea that more complex geometries will require a more flexible grid generation technology. The purpose of this paper is to show that an acoustics solution with a feedback loop can be obtained using unstructured grid technology.

The governing equations are given in Section 2. Here the nondimensionalized unsteady axisymmetric Navier-Stokes equations in conservation law form are presented. Unstructured grid generation is discussed in Section 3. The requirements of the grid for the flow solver will be explained. Also the flow code was executed on a parallel computer architecture, so the domain decomposition and message passing libraries are briefly reviewed. The unstructured based axisymmetric CE/SE method used here is briefly discussed in Section 4. Section 5 will provide the problem description with the initial and boundary condition requirements for the particular screech problems examined in this paper. In Section 6 numerical results are presented and and compared to previous numerical findings using structured grids and available experimental findings [4-8]. Conclusioning remarks will be made in Section 7.

## 2 Governing Equations

The unsteady axisymmetric Navier-Stokes equations are used to model the viscous problems in this study, since experimentally for the thin lip nozzle [4-8] with $M_j \leqslant 1.19$ the flow is axisymmetric. In nondimensionalized differential form the conservation laws are written as:

$$\boldsymbol{U}_t + \boldsymbol{F}_x + \boldsymbol{G}_y = \boldsymbol{Q}, \tag{1}$$

where $x$, $y$, and $t$ are the streamwise and radial coordinates and time, respectively. The conservative flow variable vector, $\boldsymbol{U}$, and the flux vectors in the streamwise direction, $\boldsymbol{F}$, and radial direction, $\boldsymbol{G}$, are given by:

$$\boldsymbol{U} = \begin{pmatrix} U_1 \\ U_2 \\ U_3 \\ U_4 \end{pmatrix}, \quad \boldsymbol{F} = \begin{pmatrix} F_1 \\ F_2 \\ F_3 \\ F_4 \end{pmatrix}, \quad \boldsymbol{G} = \begin{pmatrix} G_1 \\ G_2 \\ G_3 \\ G_4 \end{pmatrix},$$

with

$$U_1 = \rho, \quad U_2 = \rho u, \quad U_3 = \rho v,$$
$$U_4 = p/(\gamma - 1) + \rho(u^2 + v^2)/2.$$

Here $\rho$, $u$, $v$, $p$, and $\gamma$ are the density, streamwise velocity component, radial velocity component, static pressure, and constant specific heat ratio, respectively. The flux vectors are further split into inviscid and viscous fluxes:

$$\boldsymbol{F} = \boldsymbol{F}_i - \boldsymbol{F}_v, \boldsymbol{G} = \boldsymbol{G}_i - \boldsymbol{G}_v,$$

where the inviscid fluxes are given as:

$$F_{i1} = U_2,$$
$$F_{i2} = (\gamma - 1)U_4 + \left[(3 - \gamma)U_2^2 - (\gamma - 1)U_3^2\right]/2U_1,$$
$$F_{i3} = U_2U_3/U_1,$$
$$F_{i4} = \gamma U_2U_4/U_1 - (\gamma - 1)U_2\left[U_2^2 + U_3^2\right]/2U_1^2,$$
$$G_{i1} = U_3, \quad G_{i2} = U_2U_3/U_1,$$
$$G_{i3} = (\gamma - 1)U_4 + \left[(3 - \gamma)U_3^2 - (\gamma - 1)U_2^2\right]/2U_1,$$
$$G_{i4} = \gamma U_3U_4/U_1 - (\gamma - 1)U_3\left[U_2^2 + U_3^2\right]/2U_1^2,$$

and the viscous fluxes are:

$$F_{v1} = 0, \quad F_{v2} = \mu(2u_x - \tfrac{2}{3}\nabla\cdot\mathbf{V}),$$
$$F_{v3} = \mu(v_x + u_y),$$
$$F_{v4} = \mu[2uu_x + (u_y + v_x)v - \tfrac{2}{3}(\nabla\cdot\mathbf{V})u +$$
$$\frac{\gamma}{Pr}\frac{\partial}{\partial y}(\frac{U_4}{U_1} - \frac{u^2 + v^2}{2})],$$
$$G_{v1} = 0, \quad G_{v2} = \mu(v_x + u_y),$$
$$G_{v3} = \mu(2v_y - \tfrac{2}{3}\nabla\cdot\mathbf{V}),$$

$$G_{v4} = \mu[2vv_y + (u_y + v_x)u - \tfrac{2}{3}(\nabla\cdot\mathbf{V})v +$$

$$\frac{\gamma}{Pr}\frac{\partial}{\partial y}(\frac{U_4}{U_1} - \frac{u^2+v^2}{2})],$$

where $u, v, u_x, u_y, v_x, v_y$ are respectively the $x$ and $y$ flow velocity components and their derivatives, which can be written in terms of the conservative variables $U_1, U_2, U_3$ and $U_4$. The Prandtl number and viscosity are $Pr$ and $\mu$, respectively. The velocity divergence is

$$\nabla\cdot\mathbf{V} = u_x + v_y + v/y.$$

The source term, $\boldsymbol{Q}$, appearing on the right hand side of the equation, Eq. (1), is a result of the axisymmetric formulation and is given as:

$$\boldsymbol{Q} = \begin{pmatrix} Q_1 \\ Q_2 \\ Q_3 \\ Q_4 \end{pmatrix},$$

where

$$Q_1 = -U_3/y, \quad Q_2 = -U_2U_3/U_1y,$$

$$Q_3 = -U_3^2/U_1y, \quad Q_4 = -G_4/y.$$

Considering $(x, y, t)$ as coordinates of a three-dimensional Euclidean space, $E_3$, the Gauss divergence theorem can be used to give the following equivalent integral form of the conservation laws, Eq. (1):

$$\oint_{S(V)} \boldsymbol{H}_m \cdot \mathrm{d}\mathbf{S} = \int_V Q_m \mathrm{d}V, \qquad m = 1, 2, 3, 4, \quad (2)$$

where $S(V)$ denotes the surface of the volume $V$ in $E_3$ and $\boldsymbol{H}_m = (F_m, G_m, U_m)$ represents the total flux leaving the boundary of space-time region. The integral form of the conservation laws allows the capture of shocks and other flow discontinuities naturally. This integral form of the equations is solved numerically by the space-time conservation element and solution element method which is described in Section 4.

## 3 Grid Generation

An unstructured grid is used to show that aeroacoustics with a feedback loop can be predicted in complex domain shapes. A triangular shaped cell will be used as the geometric shape to cover a two-dimensional computational domain. The use of an unstructured grid removes the available implicit reference of the local computational neighborhood by incrementing an index as in a structured grid. Instead, the neighborhood is provided explicitly through a connectivity matrix. This connectivity matrix usually contains cell based information as well as edge based information.

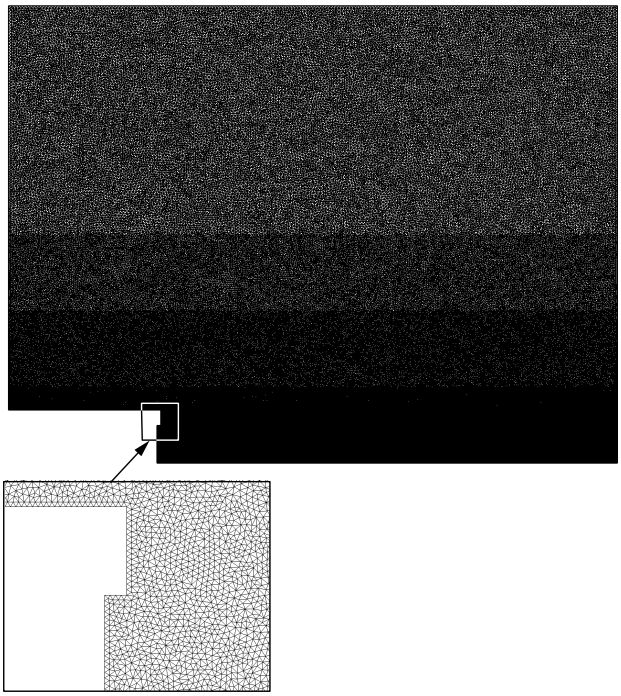

Figure 1: Triangulation of computational domain with enlargement showing nozzle lip region.

The use of a triangular unstructured grid formulation has some distinct advantages over a structured grid. One advantage to using triangular cells is that with them it is easy to generate grids about complex geometries. This reduces the amount of time required to generate a suitable grid. Also grid adaptation can be done locally without adding unnecessary cells to other regions of the domain.

The method used in this work follows a path similar to that of Holmes and Snyder [16] to triangulate a region. An example of an unstructured grid for the thin lip nozzle geometry generated in the above manner is shown in Fig. 1. The computation is axisymmetric, so only the upper half of the domain needs to be considered. An enlargement of the nozzle lip region gives an indication of the grid resolution used in these aeroacoustic feedback loop problems.

The flow code requirements dictate the type of output that the grid generation scheme must provide. A connectivity array must be generated for an unstructured grid so that a cell neighborhood is completely defined for the flow code. The code in the current work is based on a cell centered scheme. Here the triangle itself is the control volume used in the finite volume formulation.

Connectivity is determined by cell nodes, cell edges, and edge cells. Cell nodes are the nodes at the vertices of a triangle. The cell edges are the edges of a triangle

that connect those nodes. The edge cells are the cells that lie on either side of a given edge. Typically the $x$, $y$ coordinates of the cell nodes are the only grid floating point numbers required as input by a flow code. The grid connectivity is defined through integer arrays.

Boundary condition information must be defined explicitly. Ghost cells are used across boundaries such that specific boundary conditions can be applied. A boundary condition such as solid wall, inlet, exit, or any other user defined condition can be prescribed along any cell edge through the ghost cell.

For aeroacoustic problems, large numbers of cells are needed to resolve the unsteady waves. The grids are made more manageable through the use of parallel computer architecture. The publically available code METIS [17] is used to decompose the unstructured mesh into a predetermined number of subdomains so that it can take advantage of computers with multiple processors. The mesh partitioning code then load balances, minimizes the communication between processors, and minimizes the maximum number of subdomains adjacent to any other subdomain. Each processor then operates on a subset of the larger domain. It is necessary to communicate the subdomain boundary information to the neighboring processor so that the numerical algorithm can perform computations that require data from its immediate neighbor. The message passing libraries provided by the standardized package MPI [18] is used for point-to-point communication between processors. For unstructured grid based solvers a list must be maintained that provides the boundary cells so that the appropriate data may be sent and received by a processor.

A windowing technique is used to pack points in regions of the computational domain where more resolution is desired. To a limited extent the smoothness of the grid is sacrificed for an increase in resolution using this technique. A grid generated by this method will be referred to as windowed Delaunay point insertion (WDPI).

The unstructured grid generator Gridgen [19] is also used to generate a grid in the same domain for comparison purposes. The stretching techniques in this grid generator results in a much smoother grid than that provided by the windowing technique.

## 4 Discretization Technique

The space-time conservation element and solution element method is a finite volume method where the elements include space and time coordinate dimensions. The original two-dimensional CE/SE method was derived for triangular space-time grids. To date the grids used in computing the aeroacoustics from jet flows using this method have been triangulated structured grids. Here the method is applied to more general unstructured grids generated by the Delaunay method described in the previous section. In this section a general review of the CE/SE method is given as it is applied to jet noise calculations.

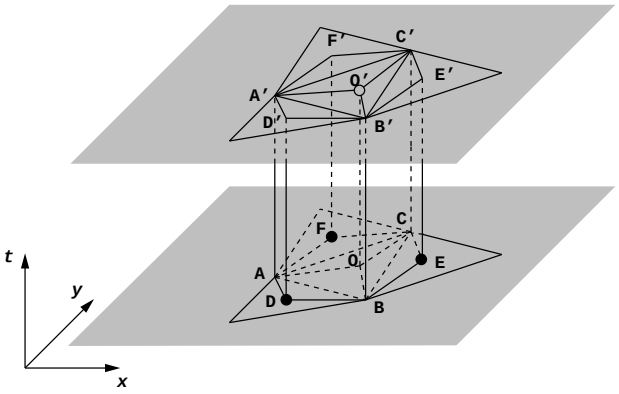


Figure 2: Conservation elements used for updating solution.

There are three conservation elements (CE's)that are associated with a given triangular space-time element, Fig. 2. The three conservation elements are shared geometrically by the three adjacent triangular space-time elements. The geometric center of the triangular faces adjacent to face $\Delta ABC$ are shown as points $D$, $E$, and $F$. Each conservation element has six faces that form a quadrilateral cylinder in space-time. The bottom and top faces are formed by connecting the centroids of the triangular bottom and top faces (of the space-time triangular element) to the nodes that make up that face, respectively. For a given space-time triangular element, this construction produces three quadrilateral faces on each of two spatial planes (i.e., $A, D, B, O$). These are nonoverlapping elements. For a given space-time triangular cylinder, the union of the three conservation elements forms a hexagonal cylinder of volume $V$ (the lower face of this hexagonal cylinder is composed of nodal points $A, D, B, E, C, F$). The conservation law Eq. (2) is applied to this hexagonal cylinder. The resulting solution is associated with the center of the hexagon at the new time level (not necessarily coincident with $O'$).

The solution elements (SE) used here are the interfaces of the conservation elements that form the hexagonal cylinder, Fig. 2.

The integral equation, Eq. (2), will provide a solution at the geometric center of the top hexagonal face. This does not necessarily coincide with the triangle cell center (the solution element) location, $E$. Discretization of the integral conservation laws, Eq. (2) leads to

$$\sum_{S(V)} \boldsymbol{H}_m^* \cdot \Delta \mathbf{S} = V(Q_m)_j^{n+1}, \tag{3}$$

for $m = 1, 2, 3, 4$, where the space-time flux at the surface centers of $S(V)$, $\boldsymbol{H}^*_m = (F^*_m, G^*_m, U^*_m)$, can be obtained. The source term on the right-hand side of Eq. (3) is computed at the center of the hexagon $A'D'B'E'C'F'$ at the new time level.

To evaluate the resulting system of algebraic equations, Eq. (3), the values must be computed at the solution element faces (actually the face centers). These face centered values are approximated by the linear Taylor series expansions. The unknowns in the integral equation, Eq. (3), are located at the cell center of the hexagon associated with $O'$. Expanding the integral equation for a given space-time element results in 12 scalar equations for the 12 unknowns at $O'$. Each of the three conservation elements contributes four scalar equations. More details of the solution method can be found in [14].

The simple non-reflecting boundary conditions described previously [20,21, 15] still work well with a Delaunay based unstructured grid. The weighted $a - \epsilon$ CE/SE scheme is used in this work. To suppress wiggles around shocks the flux derivatives use a weighted average similar to that of van Albada [22]. Details are provided in [14].

The source term evaluation was presented in a previous paper [15]. Briefly, the source term $\boldsymbol{Q}$ is a function of the unknown $\boldsymbol{U}$; therefore, a local Newton iterative procedure is needed. The procedure takes about 2-3 iterations to converge.

A simplified implicit LES procedure similar to those used in [23] is adopted here to account for the strong momentum exchange in the shear layer. In the LES, a simple Smagorinsky subgrid scale model is used for the eddy viscosity:

$$\mu_t = (C_s \Delta)^2 (2 S_{ij} S_{ij})^{1/2},$$

where

$$S_{ij} = \tfrac{1}{2}(\frac{\partial u_i}{\partial x_j} + \frac{\partial u_j}{\partial x_i}),$$

with $\Delta = (\Delta x \Delta y)^{1/2}$ and $C_s = 0.1$. Then, $\mu + \mu_t$ replaces $\mu$ in the actual computation. In practice, the LES model was only applied for radii less than $1.5D$ and $4D$ downstream of the nozzle exit plane.

## 5 Problem Description

The physical domain of interest for the screech problem is shown in Fig. 3. A slice of the axisymmetric domain shows the thin and thick lip nozzle geometries and the near-field boundaries where boundary conditions are specified in the flow code. The circular jet flow enters through the nozzle from the left and expands into the stationary ambient atmosphere. The flow condition specified at the nozzle exit at the start of the computations is choked.

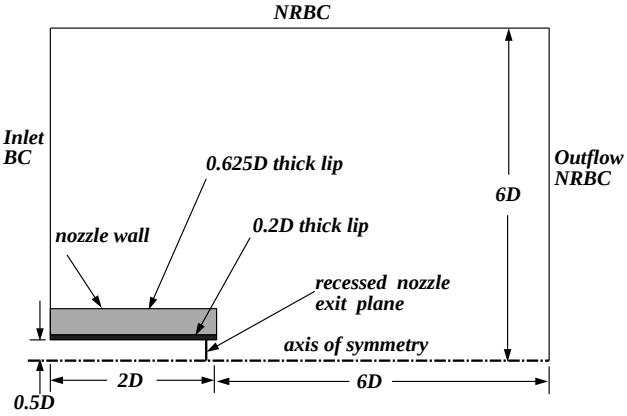


Figure 3: Geometry of the computational domain.

Here we are interested in predicting the source of the noise rather than its propagation into the far-field. The diameter, $D$, of the jet nozzle is chosen as the length scale. The density, $\rho_0$, speed of sound, $a_0$, and temperature, $T_0$, in the ambient flow are taken as scales for the dependent variables.

The Delaunay grid generator is used to cluster the triangular cells near the nozzle lip to provide good resolution for the shock cells and the acoustic feedback loop path. Cell stretching is used for these computations. We will compare flow solutions computed on a Delaunay based unstructured grid, described in Section 3 of this paper, with those previously computed on a triangulated structured grid [15]. The triangulated structured mesh is constructed by dividing each rectangular cell of the structured mesh into four triangles. An unstructured connectivity matrix is then produced. More specifics about the numbers of cells and flow code parameters will be provided in the the results section of this paper.

To clearly display the upstream propagating screech waves, the computational domain was extended $2D$ upstream of the nozzle exit. The full computational domain is a circular cylinder of $8D$ axial length and $6D$ radius. At the nozzle exit, the inflow plane is recessed by two cells so as not to numerically restrict or influence the feedback loop. The first nozzle geometry definition follows that given by Ponton *et al.* [8] where a straight nozzle lip of $0.2D$ in thickness is adopted. The second nozzle geometry has the same computational domain, however the nozzle lip thickness is increased to $0.625D$. The computational domain is modified by extending the upstream, downstream, and radial boundaries by $2D$ to determine if the boundary locations has an effect on the solutions. However, no discernible effect is realized. Only one case was used to test the effect of the extended computational domain.

### 5.1 Initial Conditions

Initially, the flow in the computation domain is set to ambient flow conditions, *i.e.*, (using nondimensional variables)

$$\rho_0 = 1, \quad p_0 = \frac{1}{\gamma}, \quad u_0 = 0, \quad v_0 = 0.$$

### 5.2 Boundary Conditions

At the inlet boundary, the conservative flow variables and their spatial derivatives are specified to be those of the ambient flow, except at the nozzle exit, where an elevated pressure is imposed, *i.e.*, the jet is under-expanded, as in the physical experiments. By using the ideal gas isentropic relations, it follows that the nondimensional flow variables at the nozzle exit, with $M_e = 1$, are given by

$$\rho_e = \frac{\gamma(\gamma+1)p_e}{2T_r},$$

$$p_e = \frac{1}{\gamma}\left[\frac{2+(\gamma-1)M_j^2}{\gamma+1}\right]^{\frac{\gamma}{\gamma-1}},$$

$$u_e = \left(\frac{2T_r}{\gamma+1}\right)^{1/2}, \qquad v_e = 0,$$

where $T_r$ is the reservoir (plenum) temperature. We will also follow the experimental cold-flow condition where the reservoir temperature is set to the ambient temperature, *i.e.*, $T_r = 1$.

At the symmetry axis, *i.e.*, $y = 0$, a simple reflective boundary condition is applied. At the top and outflow boundaries, the Type I and Type II CE/SE non-reflecting boundary conditions as described in the next subsection are imposed, respectively. The no-slip boundary condition is applied on the nozzle walls.

### 5.3 Non-Reflecting Boundary Conditions

In the CE/SE scheme, non-reflecting boundary conditions (NRBC) are constructed to allow fluxes from the interior domain of a boundary $CE$ to smoothly exit the domain. There are various implementations of the non-reflecting boundary condition and in general they have proven to be well suited for aeroacoustic problems [15]. The following NRBCs are employed in this paper.

For a grid node $(j, n)$ lying on the outer radius of the domain, the non-reflective boundary condition (Type I) requires that

$$(\boldsymbol{U}_x)_j^n = (\boldsymbol{U}_y)_j^n = 0,$$

while $\boldsymbol{U}_j^n$ is kept fixed at its initial steady boundary value. At the downstream boundary, where there are substantial gradients in the radial direction, the non-reflective boundary condition (Type II) requires that

$$(\boldsymbol{U}_x)_j^n = 0,$$

while $\boldsymbol{U}_j^n$ and $(\boldsymbol{U}_y)_j^n$ are now defined by simple extrapolation from the nearest interior node $j'$, *i.e.*,

$$\boldsymbol{U}_j^n = \boldsymbol{U}_{j'}^{n-1/2} \quad (\boldsymbol{U}_y)_j^n = (\boldsymbol{U}_y)_{j'}^{n-1/2}.$$

These are identical boundary condition specifications used in [15] for the results computed on a triangulated structured grid.

## 6 Results

The CE/SE method is applied to the underexpanded axisymmetric circular jet, with two nozzle lip thicknesses. The thin lip nozzle has a wall thickness of $20\%$ of the nozzle jet exit diameter. This case is used to compare the results obtained on a Delaunay based unstructured grid with experimental data [8] as well as with results previously obtained using a triangulated structured grid [15]. The flow solver for both grids is identical. The flow data is compared at a jet Mach number, $M_j$, of $1.19$. Screech frequency and sound pressure levels over a range of jet Mach numbers are also compared for this thin lip nozzle configuration. The thick lip nozzle has a wall thickness of $62.5\%$ of the nozzle jet exit diameter. This case is compared with expermental results [8] over a range of jet Mach numbers. A large number of times steps are required to achieve appropriate accuracy in the Fourier analysis of the time series data. Typically $80K$ time steps are needed to remove the initial transients from the computational domain. Then, another $330K$ time steps are required to record the time series data.

It is important to emphasize that no harmonic forcing is imposed in the numerical simulation. The initial impact of the boundary condition at the nozzle exit stimulates the jet shear layer and triggers the feedback loop that generates the screech waves.

In the following, the computed jet flow data and acoustic screech data are presented separately, and comparisons are made with available experimental results. The thin lip nozzle is examined first and comparisons are made with the experimental and the previously obtained numerical results. The results of the thick lip nozzle are then presented and compared with the experimental results.

### 6.1 Flow and Shock-Cell Structure for the Thin Lip Nozzle

For the flow data, the CE/SE method is applied to the thin lip nozzle case at a $M_j$ of $1.19$. The resulting shock cell structure for the axisymmetric flow calculation after $200K$ time steps is shown as a Schlieren (density-gradient modulus) contour plot, Fig. 4. The experimental [4] shock cell structure is shown in Fig. 5, and the numerical results show good agreement with the shock-cell structure in the experiment. For example, the shock

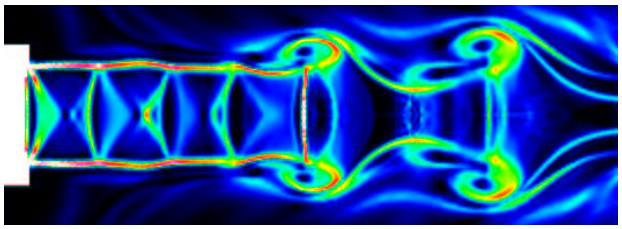

Figure 4: Instantaneous snapshot of shock cell structure for thin lip nozzle, (numerical Schlieren) $M_j = 1.19$.

Figure 5: Experimental Schlieren plot showing shock cell structure, $M_j = 1.19$.

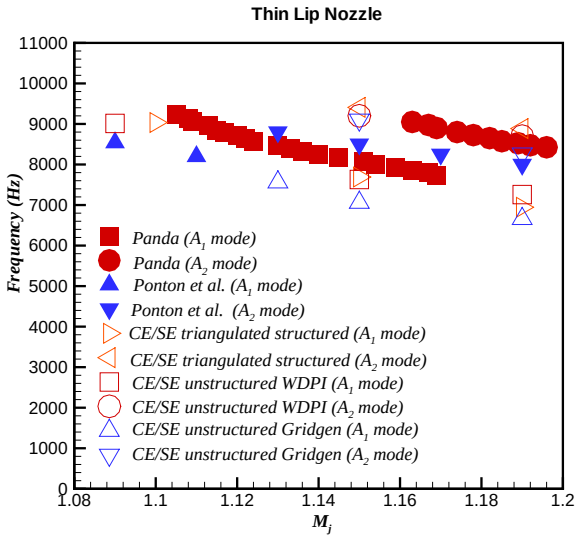


Figure 6: Frequency of thin lip nozzle over a range of $M_j$.

cell width is about $0.8D$ in the streamwise direction. In both plots, it is observed that the first two shock cells appear to be sharp and clear since the shear-layer instability wave is too weak at these locations to significantly affect the shock cell. However, it interacts strongly with the shock cells once it has gained a sufficient amplitude through its streamwise growth, which is evident by the deformation of the third and fourth shock cells. The deformation and movement of these shock cells are also seen in the experiments [4,5]. This is, as pointed out by Seiner [2], the mechanism by which the acoustic waves that produce the broadband shock-associated noise and the screech tones are generated. Furthermore, the fifth shock cell and those further downstream are so severely deformed that they almost disappear.

As demonstrated in the previous numerical results [15], the screech wave length of $1.6D$ is predicted in the computations. This is in good agreement with the experimental results (*e.g.*[4]) and the theoretical predictions of Seiner [2] and Tam [1].

The thin lip nozzle flow solution on the WDPI and Gridgen based grids compare well with the solution obtained previously on the triangulated structured grid [15]. The triangulated structured grid used a grid consisting of $132K$ cells. The WDPI grid has $167K$ cells. The Gridgen has a $136K$ cell grid. Since the flow code is the same for all of the grids presented here, there is no clear advantage to using a triangulated structured grid. In fact, a truly unstructured grid should be much more effective when the CE/SE method is applied to complex geometries.

### 6.2 Screech Frequency and Sound Pressure Level

Because the data is unsteady, many of the same techniques used to analyze experimental data are also used to analyze the numerical results. At a point on the nozzle exit lip ($x = 2.0, y = 0.642$) the time history of pressure is stored over a large number of time steps. This data is then post processed by Fast Fourier Transform (FFT) techniques to obtain spectral information.

The resulting screech frequencies are plotted over a range of jet Mach number in Fig. 6. Two experimental data sets are provided by Panda *et al.* [6] and Ponton *et al.* [8]. The nozzles in the experiments have the same diameters and operating Mach number, however they differ slightly in shape and thickness. The geometry used in the numerical predictions is that of Ponton *et al.* [8]. The CE/SE method is used to compute a solution on the same jet geometry but on three different grids. The first series of solutions are computed on the triangulated structured grid [15]. The second set of numerical data are computed on a grid generated by WDPI. This screech frequency compares quite well with that in [15]. They slightly underpredict the experimental data at the lower jet Mach numbers but they do predict the same trend. At the higher levels of $M_j$ the screech frequencies compare well with experiment.

The third set of solutions are computed on a grid generated by Gridgen [19]. The frequencies produced by the solution on the Gridgen grid are lower than those produced on the the other two grids. At a low jet Mach number, $M_j$, of 1.09 there are no detectable acoustic waves.

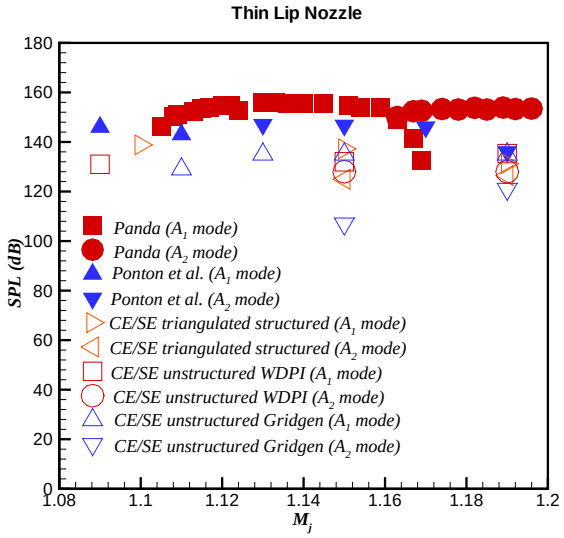


Figure 7: Sound pressure level of thin lip nozzle over a range of $M_j$.

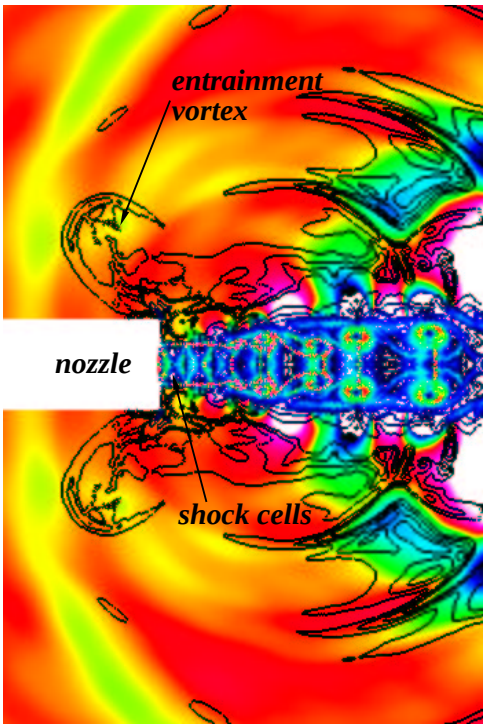


Figure 8: Instantaneous snapshot of screech wave radiation for thick lip nozzle, (isobars and Schlieren) $M_j = 1.19$. Solution shows a strong subharmonic.

The computations at the other jet Mach numbers underpredict the $A_1$ mode screech frequencies observed in the experiment, but they do predict the same trend. The $A_2$ mode screech frequencies give a close match to the experimental data.

The sound pressure level (SPL) is shown in Fig. 7. The computed results are in general lower than the experimental data. They are closer to the experimental results of Ponton *et al.* [8]. The solutions on the WDPI grid compare well with the triangulated structured grid. The solutions on the grid generated by Gridgen [19] underpredicts the SPL of the $A_2$ mode significantly. This difference could be due to the lack of resolution in that grid downstream of the nozzle.

In general it is felt that it is necessary to cluster cells in critical flow areas. The grid generated by WDPI is probably better in this case since points are forced into the region of the flow where the interaction between the shock cell and shear layer is strongest. A careful choice of $\alpha$ and time step is necessary to obtain the appropriate amount of dissipation.

### 6.3 Flow and Shock-Cell Structure for the Thick Lip Nozzle

For the thick lip nozzle case with a $M_j = 1.19$, the computed shock cell structure is shown in Fig. 8. This is an instantaneous snapshot of isobars combined with a numerical Schlieren. Unlike the thin lip nozzle case, the shock cell location which interacts with the instability wave begins between the second and third shock cell. This is much closer to the nozzle lip than is observed in the thin lip nozzle case. This is probably due to a stronger feedback mechanism due to the thick lip. Figure 8 is the larger computational domain, alluded to earlier in this paper, to test the effect of boundary location. The nozzle exit location is not changed, so the pressure data is still taken at $x = 2.0, y = 0.642$.

The thick lip case shows a strong fluid flow entrainment which produces a counter rotating vortex just upstream of the nozzle lip, Fig. 8. This entrainment vortex is observed for over $500K$ time steps. The location of the vortex practically does not move. The vortex passes cleanly through and breaks the acoustic waves as they move upstream.

A strong subharmonic wave is observed in this calculation. It propagates from a region in the flow where the pairing of vortices occurs and out through the upstream boundary. The subharmonic wave is also split by the entrainment vortex. Due to the two-dimensional axisymmetric aspect of the computation, the subharmonic wave may be much stronger than the physical one.

The total number of grid cells for the WDPI grid is $184K$ cells. The grid is clustered in the region of the nozzle lip using the windowing technique described earlier. The Gridgen grid contains $140K$ cells. This grid is also clustered but with smoother results than that given by windowing. Figure 8 has $250K$ cells with grid clus-

tering in the vicinity of the nozzle lip.

For this geometry an $\alpha$ of $0.5$ is used for the WDPI solution with a time step of $0.0005$. Any larger time step requires a correspondly larger $\alpha$ to the point where it affects the acoustic solution. The Gridgen based solution still could be run with an $\alpha$ of $1.0$ and a time step size of $0.002$.

### 6.4 Screech Frequency and Sound Pressure Level

The FFT is used to analyze the unsteady feedback loop that is generated between the shock cell structure and the nozzle lip. The pressure history is recorded over a large number of time steps, Fig. 9. The pressure level is recorded every twentieth time step after a time period such that the start-up transients have washed out of the computational domain. Figure 9 represents the time trace of pressure (nondimensional) at the point on the nozzle exit lip, $x = 2.0, y = 0.642$ for a $M_j = 1.15$ using the WDPI grid. This signal is then analyzed by FFT. The resulting SPL spectrum is shown in Fig. 10, where only the frequency range of $0$ to $20000$ *Hz* is displayed. There are two SPL spikes in the spectrum that correspond to estimated screech frequencies of $7195$ *Hz* (SPL = 142dB, $A_1$ mode) and $9169$ *Hz* (SPL = 136dB, $A_2$ mode) with a binwidth (or bandwidth) of $326$ *Hz*. This indicates that there is either two screech tone frequencies occurring at the same time or that screech mode switching is present. A strong subharmonic is also shown in this case.

The screech frequencies at the lower jet Mach numbers matched the results of Ponton et al. [8] very well, Fig. 11. At higher jet Mach numbers, $M_j = 1.15, 1.17$, and $1.19$, the screech frequencies are overpredicted.

The sound pressure levels for the thick lip nozzle in the experiment has a higher level for the $A_2$ mode than for the $A_1$ mode, Fig. 12. This is not seen in the numerical predictions.

A major advantage of the grid produced by Gridgen is that it requires less input from the user than does the WDPI grid. The grid resolution could be augmented considerably in the feedback region of the flow domain with proportionately better results. The smoothness characteristics of the Gridgen grid may also play an important role in getting a better solution.

The axisymmetric computation may be predicting a much larger subharmonic frequency than would be seen in an experiment or in a three-dimensional computation. This may be due in part to the fact that the flow is being artificially confined as axisymmetric.

## 7 Concluding Remarks

In this paper, the unstructured CE/SE Navier-Stokes method is applied to underexpanded supersonic axisymmetric jets over a range of jet Mach numbers for thin lip

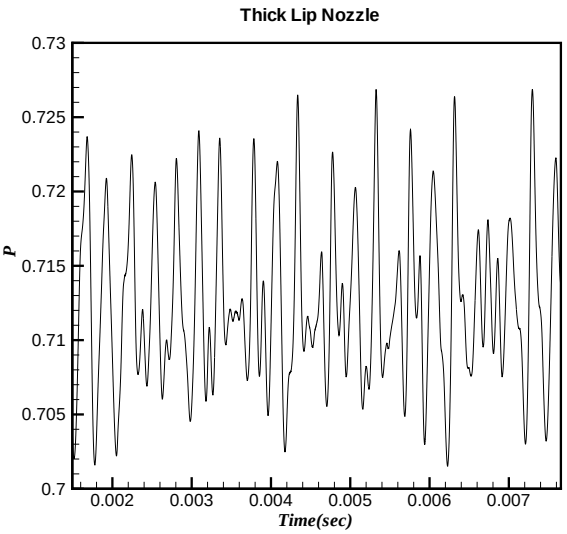


Figure 9: Time history of unsteady nondimensional pressure at nozzle exit ($x = 2.0, y = 0.642$), $M_j = 1.15$.

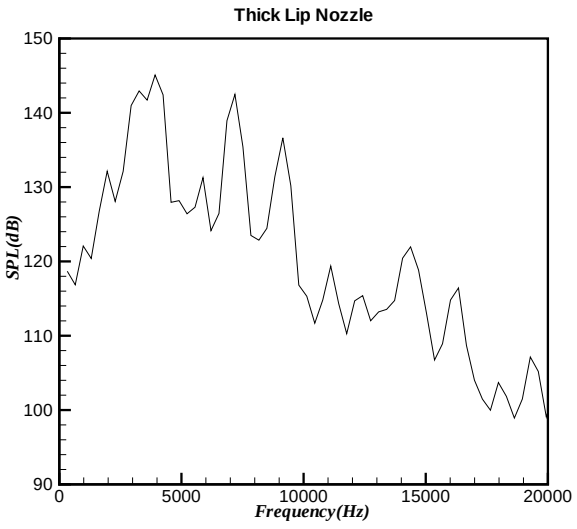


Figure 10: Sound pressure level at nozzle exit ($x = 2.0, y = 0.642$), $M_j = 1.15$, $326$ *Hz* binwidth. Note the strong subharmonics to the left.

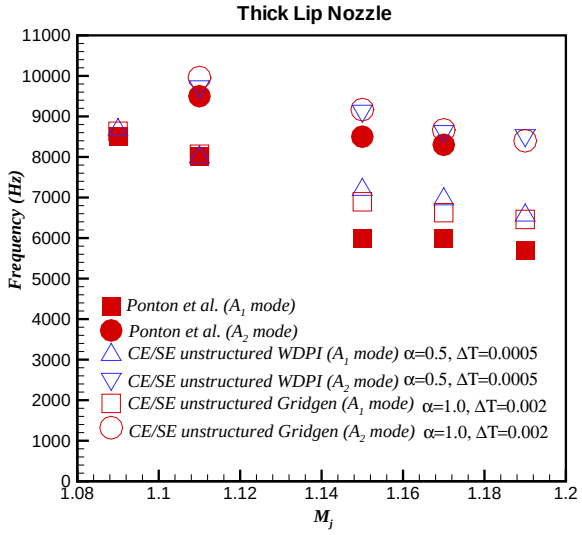


Figure 11: Frequency of thick lip nozzle over a range of $M_j$.

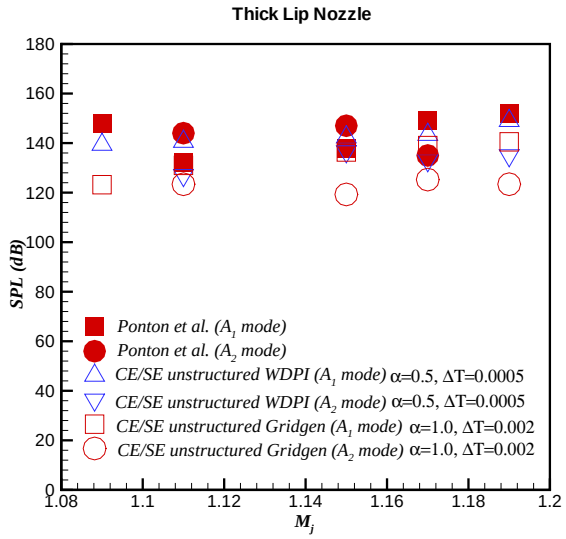


Figure 12: Sound pressure level of thick lip nozzle over a range of $M_j$.

and thick lip nozzle geometries. The resulting screech tones are analyzed.

Truly unstructured grids instead of triangulated structured grids are used to show the flexibility of the CE/SE method and to test its crucial capability of using unstructured grids to capture the physics in aeroacoustic problems with a feedback loop. The shock cell structure and many acoustic aspects of the flows compare well with the available experimental data, [4-8] and previous numerical results, [15] including the variation of screech frequency with jet Mach number for the $A_1$ and $A_2$ modes.

The thick lip case shows a strong fluid flow entrainment which produced a counter rotating vortex just upstream of the nozzle lip. This vortex is not seen in the thin lip case.

The difference in the total number of computational cells used for a given domain by the solver with a triangulated structured grid and the truly unstructured grid is not significant, so it is possible to consider aeroacoustic problems with more complex geometries using truly unstructured grids. Great care must be exercised in generating an unstructured grid. There were several cases where lack of appropriate grid resolution in critical regions of the computational domain produced a flow solution but no acoustics.

It is necessary to control the grid clustering to capture the aeroacoustics in these jet flows with a feedback loop. Grid qualities like smoothness, size, and shape, are important for the dissipative aspects of the numerical method.

## Acknowledgements

This work was supported by the Supersonic Propulsion Technology Program at the NASA John H. Glenn Research Center, Lewis Field.

## References

[1] Tam, C. K .W., "Supersonic Jet Noise," Ann. Rev. Fluid Mech. vol. 27, pp. 17-43 (1995).

[2] Seiner, J. M., "Advances in High Speed Jet Aeroacoustics," AIAA Paper 84-2275 (1984).

[3] Tam, C. K. W., "Jet Noise Generated by Large Scale Coherent Motion," NASA RP-1258, pp. 311-390 (1991).

[4] Panda, J., "Shock Oscillation in Underexpanded Screeching Jets," *J. Fluid Mech.*, vol. 363, pp. 173-198 (1998).

[5] Panda, J., "An Experimental Investigation of Screech Noise Generation," *J. Fluid Mech.*, vol. 378, pp. 71-96 (1999).

[6] Panda, J., Raman, G. and Zaman, K. B. M. Q., " Underexpanded Screeching Jets from Circular, Rectangular and Elliptic Nozzles," AIAA paper 97-1623 (1997).

[7] Panda, J. and Seasholtz, R.G, "Measurement of Shock Structure and Shock-Vortex Interaction in Underexpanded Jets Using Rayleigh Scattering," *Phys. Fluids*, vol. 11, pp. 3761-3777 (1999).

[8] Ponton, M. K., Seiner, J. M. and Brown, M. C., " Near Field Pressure Fluctuations in the Exit Plane of a Choked Axisymmetric Nozzle," NASA TM 113137 (1997).

[9] Shen, H. and Tam, C. K. W., "Numerical Simulation of the Generation of Axisymmetric Mode Jet Screech Tones," AIAA Paper 98-0283 (1998).

[10] Shen, H. and Tam, C. K. W., " Three-Dimensional Numerical Simulation of the Jet Screech Phenomenon," AIAA Paper 2001-0820 (2001).

[11] Chang, S. C., "The Method of Space-Time Conservation Element and Solution Element—A New Approach for Solving the Navier-Stokes and Euler Equations," Journal of Computational Physics. vol. 119, pp. 295-324 (1995).

[12] Chang, S. C., Yu, S. T., Himansu, A., Wang, X. Y., Chow, C. Y. and Loh, C. Y., "The Method of Space-Time Conservation Element and Solution Element—A New Paradigm for Numerical Solution of Conservation Laws," *Computational Fluid Dynamics Review*, eds. M. M. Hafez and K. Oshima, Wiley (1997).

[13] Chang, S.-C., Wang, X.-Y. and Chow, C.-Y., "The Space-Time Conservation Element and Solution Element Method—A New High Resolution and Genuinely Multidimensional Paradigm for Solving Conservation Laws," J. Comp. Phys. vol. 159, pp. 89-136 (1999).

[14] Wang, X.-Y. and Chang S.-C., " A 2-D Non-splitting Unstructured Triangular Mesh Euler Solver Based on the Space-Time Conservation Element and Solution Element Method," C.F.D. J. vol. 8, pp309-325 (1999).

[15] Loh, C. Y., Hultgren, L. S., and Jorgenson, P. C. E., "Near Field Screech Noise Computation for an Underexpanded Supersonic Jet by the CE/SE Method," AIAA Paper 2001-2252 (2001).

[16] Holmes, D. G., and Snyder, D. D., "The Generation of Unstructured Triangular Meshes Using Delaunay Triangulation," *Numerical Grid Generation in Computational Fluid Mechanics '88*, Pineridge Press, Miami, 1988. pp 643-652.

[17] Karypis, G., and Kumar, V., "Multilevel *k*-way Partitioning Scheme for Irregular Graphs," University of Minnesota, Department of Computer Science/Army HPC Research Center., Technical Report 95-064.

[18] Message Passing Interface Forum, "MPI: A Message Passing Interface Standard," International Journal of Supercomputer Applications, Vol. 8, no. 3/4, pp. 165-414, 1994.

[19] Gridgen Version 13, User Manual, Pointwise, Inc., 1998, Bedford, Texas.

[20] Loh, C. Y., Hultgren, L. S. and Chang S.-C., "Computing Waves in Compressible Flow Using the Space-Time Conservation Element Solution Element Method," AIAA J., Vol. 39, pp. 794-801 (2001).

[21] Loh, C. Y., Hultgren, L. S., Chang, S.-C. and Jorgenson, P. C. E., "Vortex Dynamics Simulation in Aeroacoustics by the Space-Time Conservation Element Solution Element Method," AIAA Paper 99-0359 (1999).

[22] van Albada, G. D., van Leer, B., Roberts, W. W., "A Comparative Study of Computational Methods in Cosmic Gas Dynamics," Astronomy and Astrophysics., Vol. 108, pp. 76-84, 1982.

[23] Bogey, C., Bailly, C. and Juvé, D., "Computation of the Sound Radiated by a 3-D Jet Using Large Eddy Simulation," AIAA Paper 2000-2009 (2000).